

Article

The Characteristic Development of Micropores in Deep Coal and Its Relationship with Adsorption Capacity on the Eastern Margin of the Ordos Basin, China

Tao Wang ^{1,2,3}, Fenghua Tian ⁴, Ze Deng ^{2,3,*}  and Haiyan Hu ^{5,*}

¹ School of Geosciences, Yangtze University, Wuhan 430100, China

² PetroChina Exploration and Development Research Institute, Beijing 100083, China

³ CNPC Unconventional Key Laboratory, Beijing 100083, China

⁴ PetroChina Coal Bed Methane Co., Ltd., Beijing 100028, China

⁵ School of Resource and Environment, Yangtze University, Wuhan 430100, China

* Correspondence: dengze@petrochina.com.cn (Z.D.); hyhucom@163.com (H.H.)

Abstract: The accurate description of micro-/nanopores in deep coal reservoirs plays an important role in evaluating the reservoir properties and gas production capacity of coalbed methane (CBM). This work studies nine continuous samples of high-rank coal from the Daning–Jixian area of the Ordos Basin. Maceral analysis, proximate analysis, field emission scanning electron microscopy (FE-SEM), low-pressure CO₂ adsorption (LPA), low-temperature N₂ adsorption (LTA) and high-pressure methane adsorption (HPMA) experiments were conducted for each sample. The fractal dimension (D) of the LPA data was calculated by using the micropore fractal model. The characteristics of the deep coal reservoir pore structure, proximate analysis, relationship between maceral and fractal dimensions, and gas adsorption capacity of the micropores are discussed. The results showed that the combination of LPA with nonlocalized density functional theory (NLDFT) models and LTA with NLDFT models can more accurately determine the pore size distribution of the micropores. The pore volume (PV) and specific surface area (SSA) of the coals were distributed in the ranges of 0.059~0.086 cm³/g and 204.38~282.42 m²/g, respectively. Although the degree of micropore development varies greatly among different coal samples, the pore distribution characteristics are basically the same, and the PV and SSA are the most developed in the pore size range of 0.4–0.7 nm. Ash content (A_d) and mineral composition are two major factors affecting micropore structure, but they have different impacts on the fractal dimension. The higher the vitrinite content, moisture content (M_{ad}) and A_d are, the larger the micropore fractal dimension (D) and the stronger the heterogeneity of the pore structure. Micropores account for 99% of the total SSA in coal, and most methane can be adsorbed in micropores. The fractal dimension of micropores can be used to evaluate the pore structure characteristics. The larger the fractal dimension, the smaller the micro-SSA and micro-PV of the coal sample. Fractal analysis is helpful to better understand the pore structure and adsorption capacity of CBM reservoirs.



Citation: Wang, T.; Tian, F.; Deng, Z.; Hu, H. The Characteristic Development of Micropores in Deep Coal and Its Relationship with Adsorption Capacity on the Eastern Margin of the Ordos Basin, China. *Minerals* **2023**, *13*, 302. <https://doi.org/10.3390/min13030302>

Academic Editors: Jianjun Liu, Yuewu Liu, Zhengming Yang, Yiqiang Li, Fuquan Song, Rui Song, Yun Yang and Saiied Aminossadat

Received: 13 December 2022

Revised: 21 January 2023

Accepted: 16 February 2023

Published: 21 February 2023

Keywords: coalbed methane; gas adsorption; micropores; pore structure distribution; eastern Ordos Basin

1. Introduction

Coal, as a strong heterogeneous porous medium, has a complex pore structure and has been widely studied [1,2]. According to the International Union of Pure and Applied Chemistry (IUPAC) classification of pores in porous materials, pores can be divided into micropores (<2 nm), mesopores (2–50 nm) and macropores (>50 nm) [3]. Some researchers had speculated that most gas in coal may be adsorbed in the micropores [4–6]. CBM mainly exists on the surfaces of micropores in the adsorbed state and connected pore and fracture systems as gas migration and transmission channels [7–9]. CBM is produced continuously through desorption, diffusion and seepage, and the diffusion and seepage that occur in


Copyright: © 2023 by the authors. Licensee MDPI, Basel, Switzerland. This article is an open access article distributed under the terms and conditions of the Creative Commons Attribution (CC BY) license (<https://creativecommons.org/licenses/by/4.0/>).

micropores are the initial stages of gas desorption and migration. In the development of CBM, more attention is drawn to the influence of the development scale and connectivity of larger fractures (macroscopic fractures) on reservoir permeability, but the development characteristics and connectivity of micropores may restrict and potentially affect CBM desorption and migration [9–12].

The pore-related characteristics of coal include the porosity, specific surface area (SSA), pore volume (PV), pore size distribution (PSD) and pore connectivity. The development scale and distribution characteristics of pore fissure in coal reservoir determine the adsorption and seepage capacity of CBM. The fine characterization of the development scale, structure and distribution characteristics of pore in coal is the premise of studying the desorption and migration of CBM at micro scale [3,13,14]. The existing characterization methods of pore structure in coal mostly apply the characterization techniques of porous solid materials, which can be roughly divided into three categories: fluid injection, image analysis and nonfluid injection methods. The image analysis method identifies and analyses pores in coal by using micro-observation techniques, such as scanning electron microscopy (SEM), transmission electron microscopy (TEM) and atomic force microscopy (AFM), which can visualize the shape, size and distribution of pores [13,15–18]. In addition, quantitative information, such as porosity and PSD, can be further obtained by combining statistical methods; however, its accuracy depends on sample characteristics, instrument performance and human factors. The fluid injection method adopts the injection of nonwettable fluid (mercury, for example) or gas (usually N₂, CO₂ and Ar) into the sample under different pressures and then obtains the PSD, PV and SSA by applying a corresponding theoretical calculation model via the fluid injection volume [19–23]. This method is easy to operate and can obtain detailed pore information of coal rock, so it is widely used in the pore characterization of coal reservoirs. However, the fluid injection method also has some limitations, and this method is suitable for studying only open pores, not closed pores. Nonfluid injection methods mainly include nuclear magnetic resonance (NMR), small angle scattering (SAS) and computed tomography (CT); these methods are advanced and accurate, but the cost of analysis is high [10,13,24–26].

Among these experimental methods, low-pressure CO₂ adsorption (LPA) and low-temperature N₂ adsorption (LTA) are the most basic and widely used [9,27]; however, the PV and SSA of coal micropores determined by the LTA method and LPA method and different models may be contradictory and lack accurate verification [9]. For example, the PV of micropores (micro-PV) and SSA of micropores (micro-SSA) determined by the LPA method are much higher than those determined by the LTA method. The SSA and PV calculated by the Dubinin–Astakhov (DA) model are usually smaller than those calculated by the density functional theory (DFT) model, and the average pore size calculated by the DA model is slightly larger than that calculated by the DFT model [19,28–32]. Although many studies have focused on the PV and SSA of pores of different scales in coal, few studies have investigated the characteristics of pores with sizes of 0.35~2.0 nm [9,20]. In this paper, nine coal samples from the Daning–Jixian block on the eastern margin of the Ordos Basin were selected as research objects. Through LPA and LTA experiments, the micropore structure of deep coal reservoirs in the research area was analysed, and the fractal dimension of the micropores in the coal samples was calculated by using LPA data. High-pressure methane adsorption (HPMA) experiments were carried out to measure the CH₄ adsorption capacity of the coal samples. The specific objectives were (1) to analyse and compare the accuracy of the calculation results of different models (including the DA, Dubinin—Radushkevich (DR), grand canonical Monte Carlo (GCMC) and nonlocal density functional theory (NLDFT) models); (2) to explore the ratios of the PVs and SSAs of micropores and mesopores in deep coal reservoirs; (3) to discuss the factors influencing micropore fractal dimensions in deep coal reservoirs; and (4) to determine whether there is a strict correlation between the micro-SSA, micro-PV and adsorption capacity of deep coal reservoirs.

2. Geological Setting

The Ordos Basin is one of the main oil-bearing basins in China and has an area of approximately $37 \times 10^4 \text{ km}^2$ [33,34]. According to the tectonic morphology, the basin can be subdivided into 6 secondary tectonic units [8,33,35]. The study area is located in the eastern margin of the Ordos Basin, spanning Shanxi and Shaanxi provinces, in Daning County and Ji County (Figure 1a) [8]. As a part of the Ordos Basin, the study area experienced a palaeogeographic evolution process in the late Carboniferous–middle Permian, which was dominated by marine sedimentary surface continental marine facies, transitional facies and fluvial clastic sedimentary facies, during which several transgression events occurred. The study area can be divided into the Permian Shanxi Formation, Taiyuan Formation and Carboniferous Benxi Formation [34,36,37]. The lithology of the top of the Taiyuan Formation is micritic bioclastic limestone, indicating that the sedimentary water was clear seawater with normal salinity, corresponding to a typical shallow marine shelf sedimentary environment. The lower Benxi Formation was formed in coastal and shallow shelf environments, and mudstone, grey and black mudstone interbedded with thin sandstone, limestone and black coal were deposited from bottom to top. The Shanxi Formation is characterized by rapid sedimentary phase transformation and complex lithologic assemblages, and the Shanxi Formation can be divided into the lower Shan2 member and the upper Shan1 member (Figure 1b) [33,34]. The main target strata are the No. 5 coal of the Shanxi Formation, No. 8 coal of the Taiyuan Formation and No. 9 coal of the Benxi Formation, with the main body buried 2000–2400 m deep; the No. 5 coal seam has thicknesses of 1~3 m, and the No. 9 coal seam has thicknesses of 5~12 m. This seam is the main exploration target layer of deep CBM.

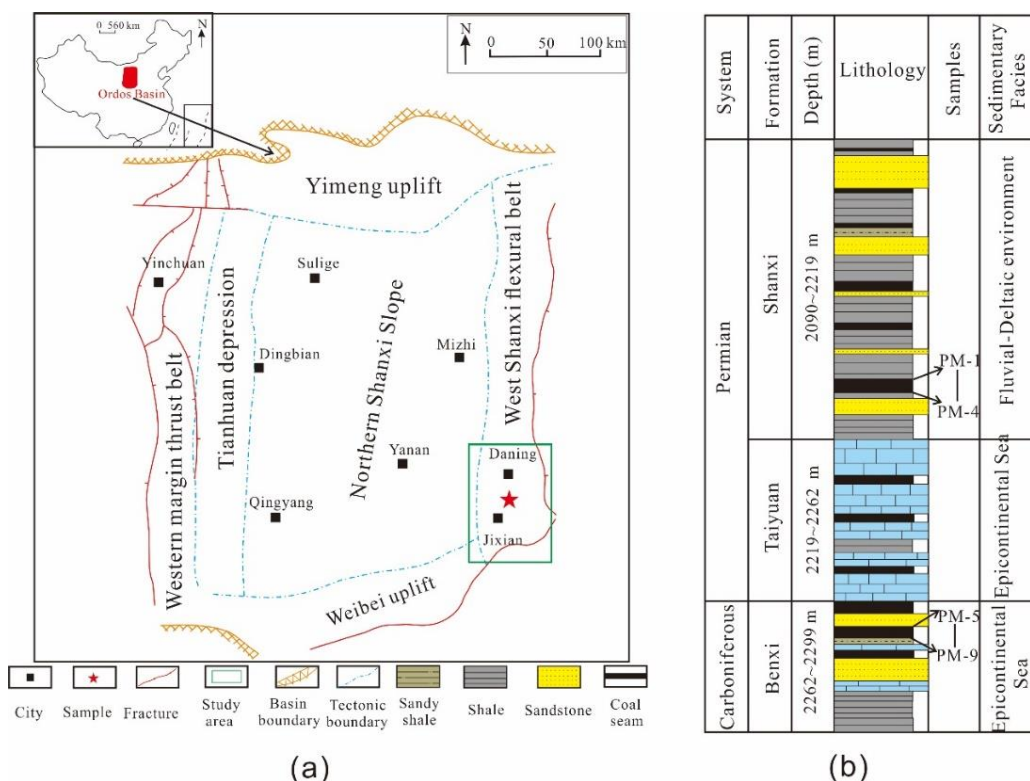


Figure 1. (a) Location of the study area. (b) Stratigraphic columns of the coal-bearing strata.

3. Samples and Experimental Methods

Nine fresh coal samples from recently drilled wells in the Daning–Jixian area on the eastern margin of the Ordos Basin were selected; the coal-bearing strata, including the Shanxi Formation and Benxi Formation, were formed in a transitional environment be-

tween land and sea. All 9 coal samples are black semi-dark coals, including 5 samples from the Shanxi Formation and 4 samples from the Benxi Formation (Figure 1b). To obtain the basic physical characteristics of the coal samples, a Leica DM4P photometer microscope was used for observations, and maximum vitrinite reflectance ($R_{o,\max}$) measurements (50 points) and maceral analyses (500 points) were carried out randomly under reflected light with oil immersion, strictly following the national standards GB/T 6948–2008 and GB/T 8899–2013, respectively. According to national standard GB/T 30732–2014, the moisture content (M_{ad}), ash content (A_d), volatile matter content (V_{daf}) and fixed carbon content (FC_{ad}) of the coal samples were analysed [38].

LPA and LTA experiments were performed using a Quantachrome Instruments Au-tosorb IQ-MP automatic gas adsorption analyser according to national standards GB/T 21650.2-2008 and GB/T 21650.3-2011. The coal and rock samples were ground with an agate mortar and screened to 60~80 mesh. The samples were weighed to approximately 2~3 g, and the test temperatures were 273 K and 77 K. An FEI Helios 650 field emission scanning electron microscopy (FE-SEM) device was used to image the coal and rock samples and observe their pore morphology. The implementation standard was China's petroleum industry standard SY/T 5162-2014. The HPMA experiments were carried out by Gravimetric Isotherm Rig 3. According to the national standard GB/T 19560-2008, the test sample size was approximately 80 g of dry sample of size 60~80 mesh, and the maximum pressure and temperature were set to 25 MPa and 70 °C, respectively.

4. Results

4.1. Coal Rock Coal Quality Characteristics

The results show that the maturity increases with increasing coalification degree. The R_o values of the collected coal and rock samples range from 2.93% to 3.30% (Table 1). The average R_o values of the Shanxi Formation and Benxi Formation are 3.13% and 3.17%, respectively, which are considered high-rank coals according to standard ISO 11760:2018. The macerals are mainly vitrinite (54.0% average), which is considered a medium vitrinite coal according to standard ISO 11760:2018, followed by inertinite (40.1% average), and exinite is not visible. The mineral group is relatively low, accounting for 2.2–9.8% of the coal rocks and are mainly clay minerals, silica, carbonate and iron sulfide (Table 1).

Table 1. Basic characteristics of coal samples.

Samples	Strata	Coal Seam	Depth (m)	$R_{o,\max}\%$	Proximate Analysis (%)				Macerals (%)		
					M_{ad}	A_d	V_{daf}	FC_{ad}	Vitrinite	Inertinite	Minerals
PM-1	Shanxi	5 #	2195.3	2.93	1.1	12.6	7.2	79.1	62.7	27.8	9.5
PM-2	Shanxi	5 #	2195.7	3.13	0.8	10.3	6.8	82.2	52.9	39.5	7.6
PM-3	Shanxi	5 #	2196.5	3.14	0.8	5.8	6.8	86.7	41.8	52.5	5.7
PM-4	Shanxi	5 #	2197	3.30	1.0	6.8	6.5	85.7	62.7	35.1	2.2
PM-5	Benxi	8 #	2274.1	3.15	1.2	12.7	7.0	79.2	52	43.9	4.1
PM-6	Benxi	8 #	2274.4	3.15	0.8	12.6	10.1	76.5	64.3	26.6	9.1
PM-7	Benxi	8 #	2275.7	3.17	0.7	7.3	6.3	85.7	34.1	61.3	4.6
PM-8	Benxi	8 #	2276.4	3.21	1.3	6.4	6.6	85.8	58	38.5	3.5
PM-9	Benxi	8 #	2277.1	3.15	1.1	8.3	7.3	83.3	57.83	35.37	6.8

Note: $R_{o,\max}$ = maximum oil vitrinite reflectance; M_{ad} = moisture content; A_d = ash content; V_{daf} = volatile matter content; FC_{ad} = fixed carbon content.

The moisture contents (M_{ad}) of the coal rocks in the Shanxi and Benxi Formations range from 0.7% to 1.3% (1.0% average). The ash contents (A_d) range from 5.8% to 12.7% (9.2% average), corresponding to a low-medium ash coal according to standard ISO 11760:2018. The volatile matter contents (V_{daf}) range from 6.3% to 10.1% (7.2% average), which is low.

The fixed carbon contents (FC_{ad}) range from 76.5% to 86.7% (82.7% average), which is very high (Table 1). When coal is ranked high, FC_{ad} is usually negatively correlated with A_d [38].

4.2. Pore Morphology Characteristics

The pore morphology of coal is clearly observable by FE-SEM. According to the origin and distribution characteristics of the pores, they can be divided into two categories: (1) organic pores, composed of gaseous pores and shrinkage pores/fractures, and (2) mineral-related pores, consisting of intraparticle (IntraP) pores within minerals and interparticle (InterP) pores between matrix particles [39,40]. Figure 2 shows the pore types of 9 representative coal samples in FE-SEM images. The results show that organic pores and InterP pores are widely distributed in the coal samples in the study area, with various shapes, abundant nanopores and a small number of microscale pores/cracks (Figure 2a,b). The gaseous pores are round, oval and slit-shaped and form a pore network (Figure 2c), which greatly increases the pore connectivity and results in a good storage capacity. The pore widths are mainly in the range of approximately 200 nm to 2.0 μm . Wang (2019) and Li (2019) et al. show that the pore shapes are generally spherical for low rank coal and they are mainly ellipsoidal for high rank coal [17,40]. High-order coal seams in the study area are buried deep (>2000 m) and have a high degree of thermal evolution; under the high pressure conditions of overlying strata, pores are compressed, forming various irregular forms such as wedges and slits (Figure 2f,h,i). In contrast to the organic matter pores, the pores in grains generally exist between mineral particles or between minerals and organic matter and are polygonal and elongated (Figure 2f,g). FE-SEM images show that the clay minerals are closely bound to the organic matter: most of the internal pores associated with the organic matter are slit-shaped and form along a clay boundary; these pores are more than 200 nm wide (Figure 2f). Among them, the clay minerals in PM-6 are vermicular and stacked, which can produce shrinkage cracks (Figure 2d,f,g). The clay minerals in the PM-9 coal sample are massive and form a large number of polygonal grain pores (Figure 2g–i).

4.3. Quantitative Analyses of Pore Structure

4.3.1. CO₂ Adsorption Isotherms

The LPA method to determine the pores in coal generally reveals monolayer adsorption or micropore filling at the <2 nm scale [41–43]. The CO₂ adsorption isotherms of the coal samples are shown in Figure 3, which show similar characteristics. Their CO₂ adsorption capacity increases steadily with increasing pressure [44]. According to the IUPAC standards, the CO₂ adsorption isotherms of coal and rock samples all have typical type I isotherm characteristics, indicating that all coal and rock samples have microporous properties. Sample PM-8 (29.9 cm³/g STP) has the highest adsorption capacity for CO₂, indicating the highest microporosity, while sample PM-1 (21.6 cm³/g STP) has the lowest adsorption capacity for CO₂, indicating the lowest microporosity.

The DA, DR, GCMC and NLDFT models in ASiQwin software were used to calculate the PV and SSA distribution of all coal and rock samples, and the results are shown in the corresponding Table 2. The SSA and PV of the same coal sample vary greatly under different models. As the DA and DR models are traditional macroscopic thermodynamic models, they are based on Polanyi potential theory and Dubinin micropore filling theory [45,46]. The PVs calculated by the DA model and DR model are 0.078~0.113 cm³/g and 0.065~0.084 cm³/g, respectively. The SSAs obtained by the DR model are 182.437~236.571 m²/g (Table 2). GCMC and NLDFT are molecular dynamics models that describe the microscopic theory of fluid adsorption and phase behaviour in narrow pores at the molecular level [47,48], the properties of adsorbed gas molecules linked to their adsorption properties in pores of different sizes. The GCMC and NLDFT models provide a more accurate method for pore size analysis. The PVs calculated by the GCMC model and NLDFT model are 0.056~0.092 cm³/g and 0.062~0.092 cm³/g, respectively, and the calculated SSAs are 187.447~277.147 m²/g and 209.408~291.810 m²/g, respectively (Table 2).

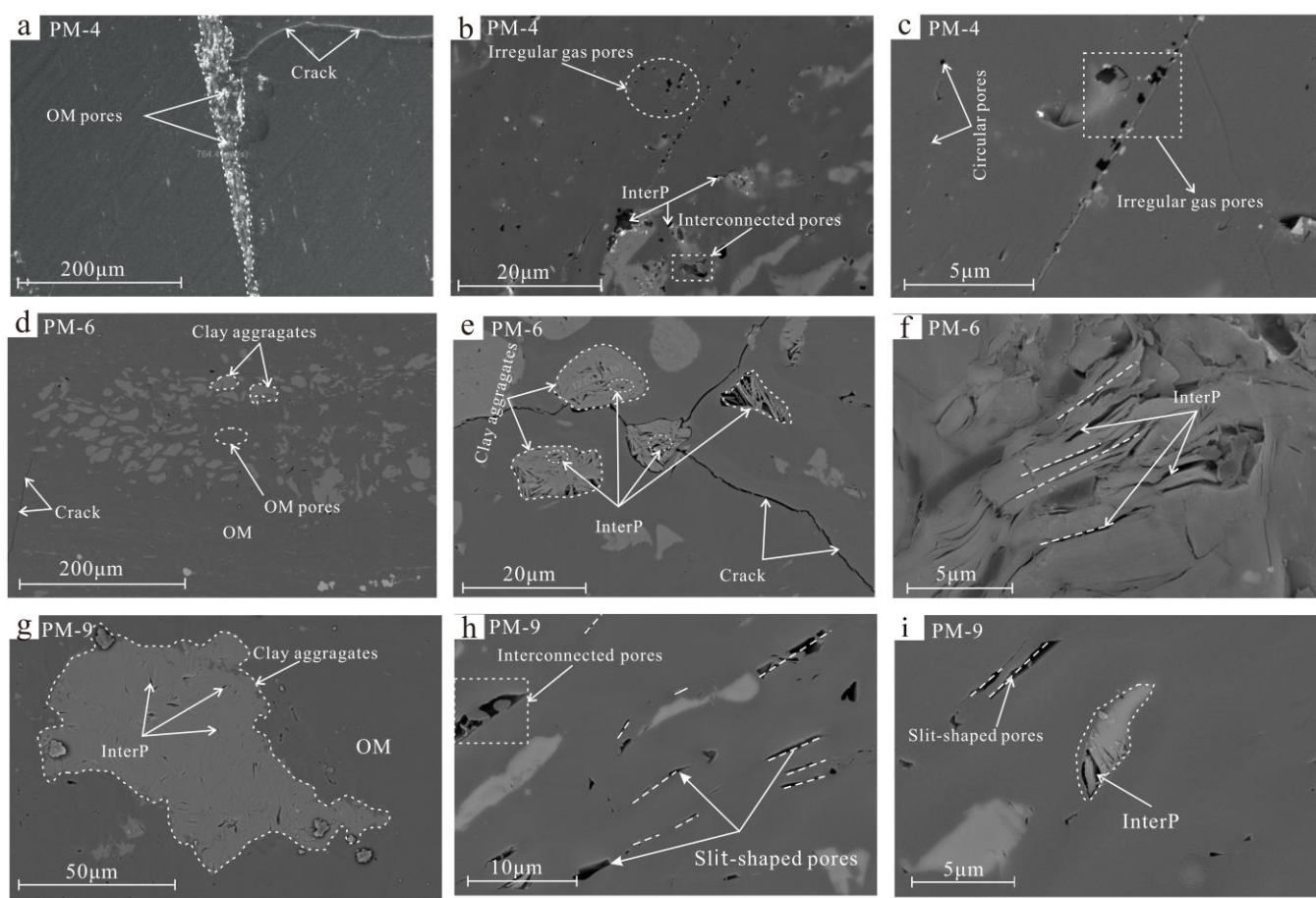


Figure 2. FE—SEM images of the organic and inorganic pores in selected coal samples. (a–c) The pore–fracture distribution and irregular gas pores, sample PM-4. (d–f) The coal matrix and clay mineral distribution and InterP pores, sample PM-6. (g–i) Directional alignment and some slit-shaped pores, sample PM-9.

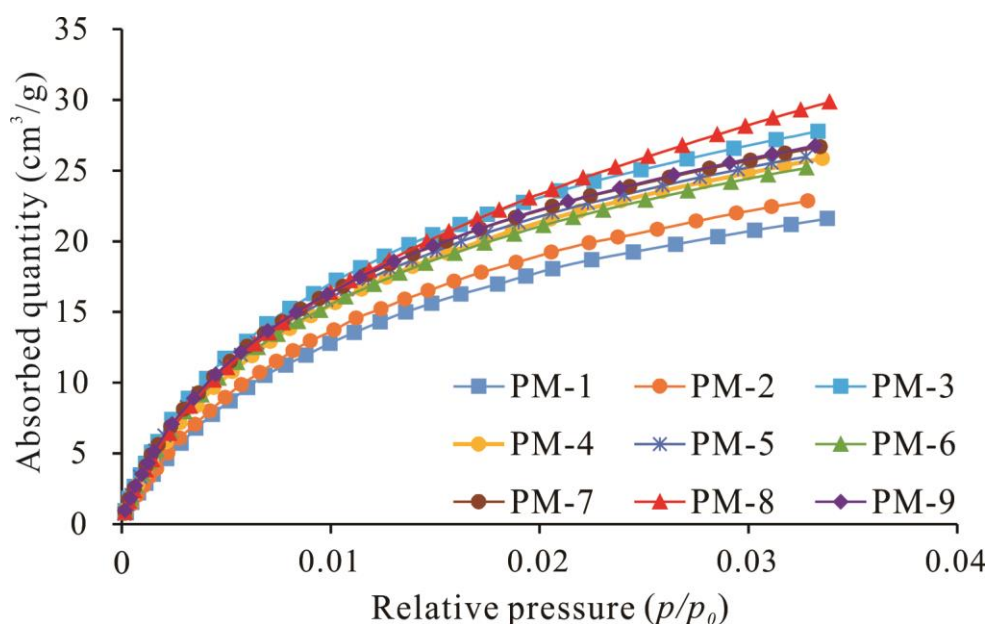


Figure 3. CO₂ adsorption isotherms obtained at 273 K for different samples.

Table 2. The PV and SSA of LP-CO₂/N₂GA calculated by different models.

Model	Parameters	PM-1	PM-2	PM-3	PM-4	PM-5	PM-6	PM-7	PM-8	PM-9	
CO ₂ adsorption	DR	PV (cm ³ /g)	0.065	0.071	0.076	0.075	0.075	0.073	0.084	0.079	0.077
		SSA (m ² /g)	182.437	199.568	214.939	212.133	211.343	204.318	236.571	222.042	216.809
	DA	PV (cm ³ /g)	0.078	0.086	0.083	0.090	0.082	0.079	0.113	0.094	0.092
		SSA (m ² /g)	187.447	205.006	236.368	227.242	238.084	230.864	277.147	250.915	244.416
	GCMC	PV (cm ³ /g)	0.056	0.063	0.070	0.068	0.073	0.071	0.092	0.076	0.075
		SSA (m ² /g)	187.447	205.006	236.368	227.242	238.084	230.864	277.147	250.915	244.416
N ₂ adsorption	NLDFT	PV (cm ³ /g)	0.062	0.066	0.079	0.078	0.077	0.075	0.092	0.081	0.079
		SSA (m ² /g)	209.408	224.502	266.137	257.523	260.323	252.787	291.810	275.762	267.185
	BET	SSA (m ² /g)	0.269	0.302	0.305	0.449	0.515	0.376	0.173	0.291	0.454
		PV (cm ³ /g)	0.002	0.001	0.001	0.002	0.003	0.002	0.001	0.002	0.001
	BJH	SSA (m ² /g)	0.638	0.557	0.451	0.873	0.835	0.688	0.458	0.558	0.613
		PV (cm ³ /g)	0.001	0.001	0.001	0.002	0.002	0.001	0.001	0.001	0.001
Total micropore	NLDFT	SSA (m ² /g)	0.388	0.349	0.337	0.522	0.592	0.449	0.281	0.390	0.414
		PV (cm ³ /g)	0.059	0.063	0.074	0.073	0.072	0.070	0.086	0.076	0.074
	SSA (m ² /g)	204.380	219.385	258.675	250.065	253.102	245.765	282.415	268.210	259.860	

Note: DR = Dubinin–Radushkevich; DA = Dubinin–Astakhov; GCMC = grand canonical Monte Carlo; NLDFT = Nonlocal density functional theory; BET = Brunauer–Emmett–Teller; BJH = Barrett–Joyner–Halenda; PV = pore volume; SSA = specific surface area.

Although the PV and SSA measured by the DA, GCMC and NLDFT models are similar, the PSD is obviously different, the PSD calculated by the GCMC model and NLDFT model has multiple peaks, and the pore sizes are mainly 0.4–0.7 nm and 0.8–0.9 nm, respectively (Figure 4). The DA calculation results show a single peak, and the pore sizes are mainly between 1.5 and 3.5 nm. Because the thermodynamic properties of fluid in micropores are very different from those in the free state, the critical point, freezing point and triple point change [9]. However, the DA and DR models do not take into account the changes in these parameters or the effect of pore shape on gas molecular aggregation, so the results calculated by these models may be more biased. Blacher et al. (2000) and El-Merraoui et al. (2000) also analysed and compared the activated carbon micropores of different models, and the results showed that the NLDFT model was more reliable due to its smaller fitting error [1,49]. Jie et al. (2018) measured isotherms and calculated the fit-ing error of isotherms by comparing different models and determined that the fitting error of the NLDFT model was smaller than that of the GCMC model [50]. Song et al. (2020) showed that the fitting curves of the DR and DA models deviated greatly from the measured isotherms, with relative errors of 27.2% and 18.4%, respectively [9]. However, the fitting curves of the GCMC and NLDFT models are basically consistent, and the relative errors are 0.37% and 0.23%, respectively. These results show that the NLDFT model is more accurate for analysing the PSD of micropores in coal under LPA.

4.3.2. N₂ Adsorption Isotherm

The LTA isotherms of the coal and rock samples are shown in Figure 5, indicating that the N₂ adsorption volumes of all coal and rock samples are within 0.79~1.97 cm³/g. According to the IUPAC classification, the main form of coal in the study area is type IV [3]. When the relative pressure $p/p_0 > 0.1$, the adsorption curve increases rapidly, indicating that these samples have a strong adsorption effect on N₂. Initially, the adsorption curve rises slowly with increasing pressure, indicating that the sample is slowly transformed from monolayer adsorption to multimolecular adsorption. When $p/p_0 \approx 1$, the capillary condensation effect leads to a sharp rise in the curve, and the coal sample does not show adsorption saturation equilibrium, indicating that there are certain large pores in the coal sample. For desorption branches, when $p/p_0 \approx 0.5$, the curve is above the adsorption branch. In addition, when $p/p_0 \approx 0.5$, the curve shows a rapid decline; after this point, the desorption branch and the adsorption branch basically coincide.

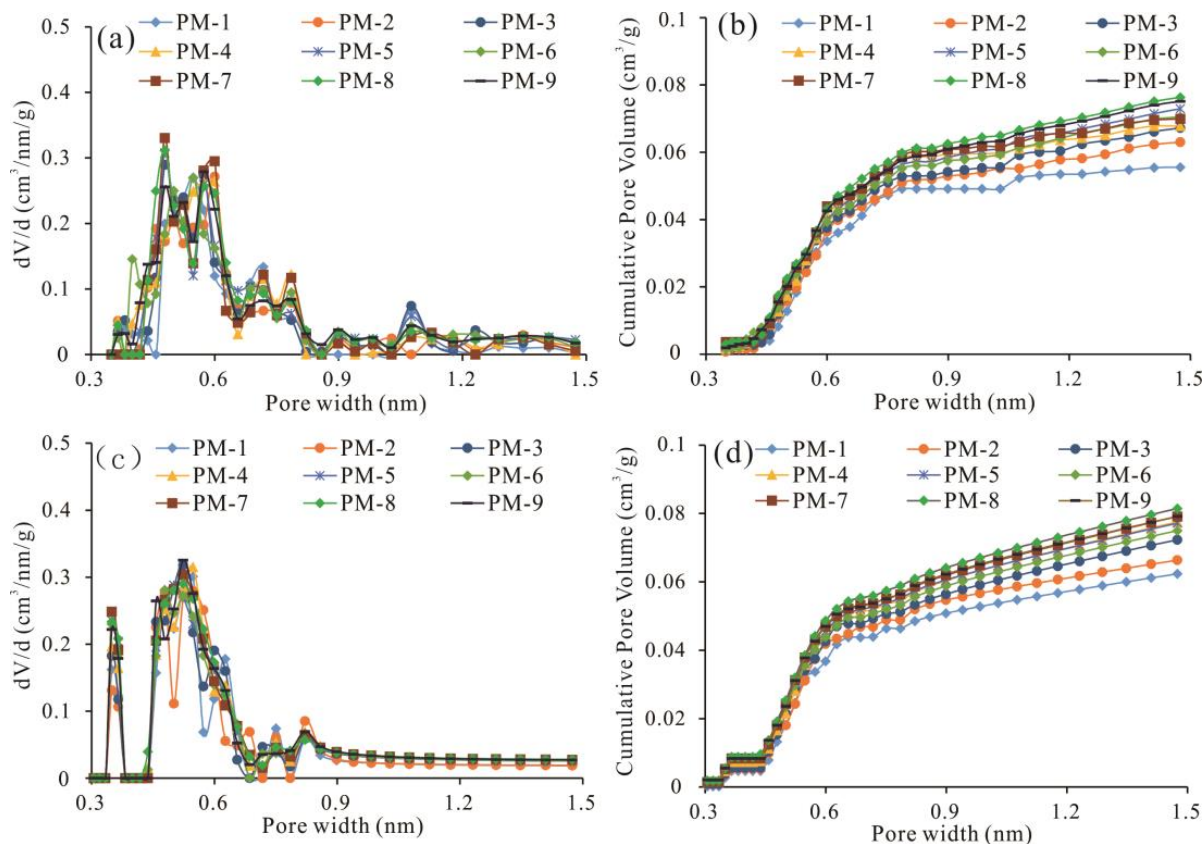


Figure 4. Distribution of the PV calculated by different models for different pores sizes. (a,b) GCMC model, (c,d) NLDFT model.

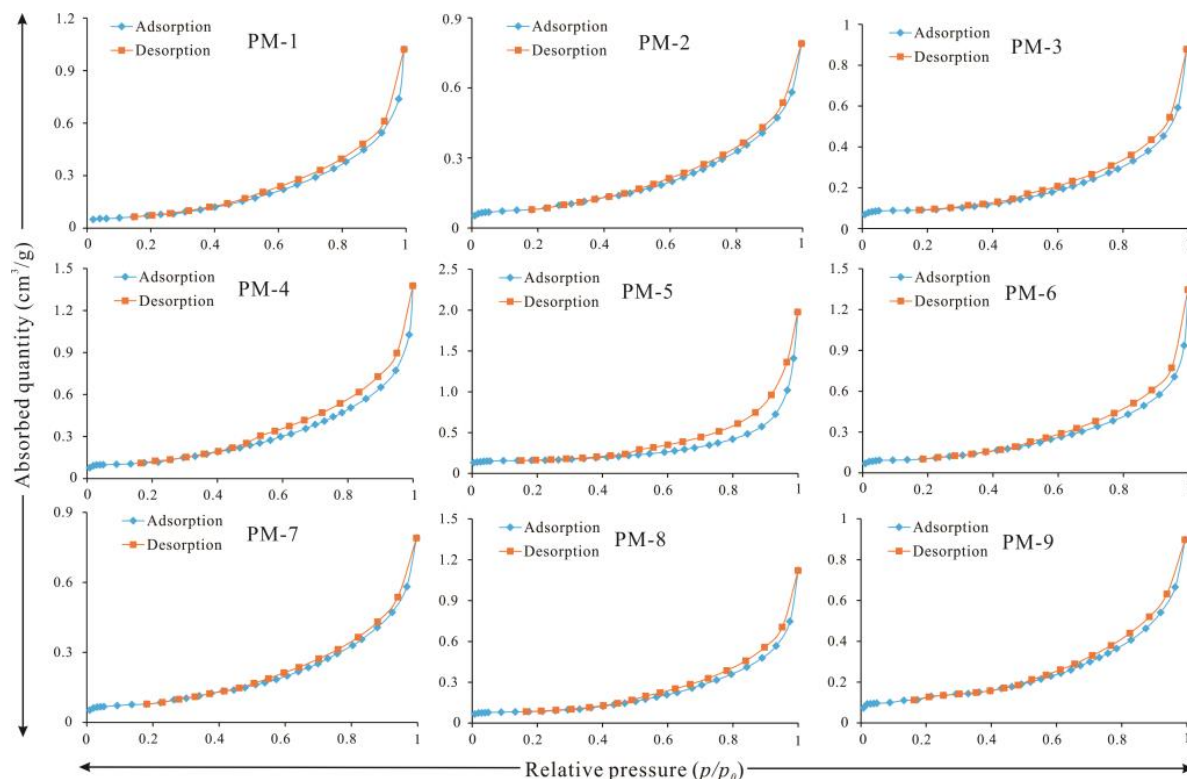


Figure 5. N_2 adsorption isotherm of ten samples at 77 K.

The shape of the hysteresis loop can yield important information about the pore structure. According to adsorption aggregation theory, different relative pressures on the same pore lead to the formation of an adsorption ring between the adsorption curve and the desorption curve during the agglomeration and evaporation processes, which are mainly caused by the complex combination of different pore morphologies [13,44,51]. Pore types can be divided by shape into cylindrical, ink bottle, parallel plate, slit, etc. According to the IUPAC classification of hysteresis loops, the hysteresis loops of the coal and rock samples in the study area are mainly classified as the H3 type (Figure 5). The hysteretic curves of all coal samples are similar to those of the H3 type. When the relative pressure is low ($p/p_0 \approx 0.5$), the adsorption and desorption curves basically coincide, indicating that the pore types are mainly cylindrical, conical and anvil-shaped. When p/p_0 is large, there is a slight hysteresis loop, indicating the existence of open pores.

ASiQwin software was used to calculate the experimental data of LTA. The Brunauer–Emmett–Teller (BET), Barrett—Joyner—Halenda (BJH) and NLDFT models were used to calculate the results, as shown in Table 2. The results of the NLDFT model and BJH model are similar (Figure 6). The BJH model and NLDFT model were used to calculate PVs of $0.001\text{--}0.003\text{ cm}^3/\text{g}$ and $0.001\text{--}0.002\text{ cm}^3/\text{g}$, respectively. The BET, BJH and NLDFT models were used to calculate SSAs of $0.173\text{--}0.515\text{ m}^2/\text{g}$, $0.451\text{--}0.873\text{ m}^2/\text{g}$ and $0.281\text{--}0.592\text{ m}^2/\text{g}$, respectively. Groen et al. (2003) and Song et al. (2020) proved experimentally and theoretically that the DFT model is more accurate than other models. Considering the fitting error and convergence of the pore size range [5,9]. Jie et al. (2018) determined that the total PV and total SSA of pores obtained by the BJH model were generally slightly higher than those obtained by the NLDFT model [50]. By comparing the fitting errors of the calculated isotherms and measured isotherms, it is determined that the fitting errors of the NLDFT model are less than those of the BJH model (Table 3) [52]. Because the anisotropy and surface roughness of nanopores are considered in the NLDFT model, it is more accurate to analyse the PSD of nanopores in coal.

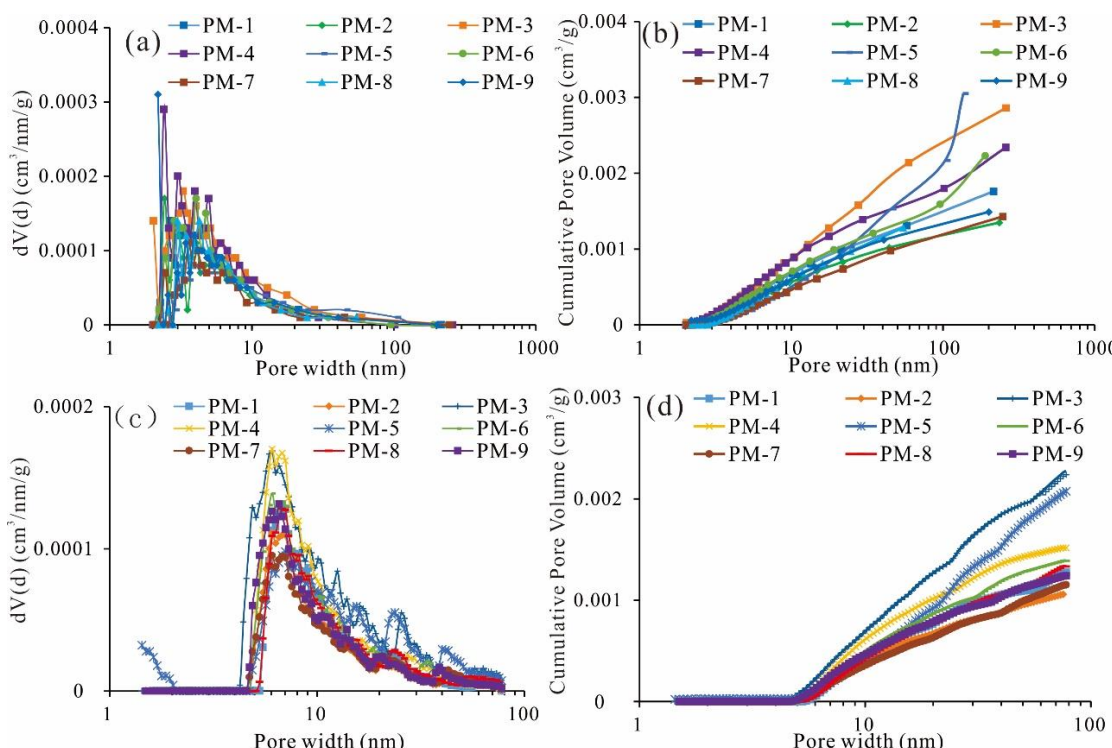


Figure 6. Distribution of the PV calculated by the BJH and NLDFT models. **(a,b)** BJH model, **(c,d)** NLDFT model.

Table 3. Pore analysis results of the BJH and NLDFT models.

Samples	Model					
	BJH			NLDFT		
	PV (cm ³ /g)	SSA (m ² /g)	Fitting Error (%)	PV (cm ³ /g)	SSA (m ² /g)	Fitting Error (%)
PM-1	0.002	0.638	1.37	0.001	0.388	0.44
PM-2	0.001	0.557	0.84	0.001	0.349	0.16
PM-3	0.001	0.451	0.48	0.001	0.337	0.11
PM-4	0.002	0.873	0.94	0.002	0.522	0.16
PM-5	0.003	0.835	0.62	0.002	0.592	0.15
PM-6	0.002	0.688	0.83	0.001	0.449	0.19
PM-7	0.001	0.458	1.65	0.001	0.281	0.62
PM-8	0.002	0.558	0.92	0.001	0.390	0.34
PM-9	0.001	0.613	0.35	0.001	0.414	0.09

Note: NLDFT = Nonlocal density functional theory; BJH = Barrett—Joyner—Halenda; PV = pore volume; SSA = specific surface area.

4.4. Pore Fractal Characteristics

Currently, the fractal dimension based on the high-pressure mercury injection method and gas adsorption method is the most commonly used method to study reservoir heterogeneity [42,53,54]. However, due to the limitation of measurement accuracy and the gas occurrence mechanism, the two methods are most applicable to the range of macro- and mesopores and cannot accurately characterize the heterogeneity of micropores. Previous studies have shown that adsorbent molecules in micropores are usually filled with micropores [55,56]. Jaroniec et al. (1993), via the adsorption test of microporous activated carbon, determined that the pore size distribution of micropores is the core factor affecting its heterogeneity [55]. According to the DA equation, the adsorption process of micropores is the filling of their inner volume rather than the layered adsorption on the pore wall. The pore packing degree θ was used to characterize the adsorption capacity:

$$\theta = \frac{n}{n_{max}} = \int_0^\infty \exp[-(Az/\beta)^3]F(z)dz, \quad (1)$$

where

$$A = RTLn(p_0/p), \quad (2)$$

and

$$z = 1/E_0. \quad (3)$$

In the above equations, θ is the packing degree of CO₂ molecules in micropores; n and n_{max} are, respectively, the amount and maximum amount adsorbed in the micropores, cm³/g; A is the adsorption potential, kJ/mol; β is a similarity constant, which is related to the adsorbent, 0.38; $F(z)$ is the normalized distribution function; E_0 is the characteristic energy, kJ/mol; p/p_0 is the relative pressure; z is the inverse of E_0 , mol/kJ; T is the absolute temperature, K; and R is the universal gas constant, 8.314 J/(mol·K). According to Jaroniec et al. (1993) [57], the normalized distribution function $F(z)$ of z is represented by a gamma distribution:

$$F(z) = \frac{3\rho^v}{\Gamma(\frac{v}{3})} \cdot z^{v-1} \cdot e^{-(\rho z)^3}, \quad (4)$$

where

$$\Gamma(x) = \int_0^\infty t^{x-1} e^{-t} dt, \quad (5)$$

where ρ and v are related parameters of the $F(z)$ distribution function; ρ is the scale parameter, kJ/mol; and v is the shape parameter. The analytical solution of the integral

Equation (1) with the gamma distribution (Equation (5)) provides a very simple expression for the overall adsorption θ :

$$\theta = \frac{n}{n_{max}} = \left[1 + \left(\frac{A}{\beta\rho} \right)^3 \right]^{-\frac{v}{3}}. \quad (6)$$

According to Stoeckli et al. (2009) [58] research results on the relationship between adsorption characteristic energy and pore size of micropores, empirical formulas for x and z can be obtained as follows:

$$x = 15z + 2852.5z^3 + 0.014z^{-1} - 0.75, \quad (7)$$

and

$$J(x) = F(z) \frac{dz}{dx}. \quad (8)$$

The combination of Equations (4), (7) and (8) provides the following expression for the micropore size distribution $J(x)$:

$$J(x) = \frac{3\rho^v}{\Gamma(\frac{v}{3})} \cdot \frac{z^{v-1} \cdot e^{-(\rho z)^3}}{15 + 8557.5z^2 - 0.014z^{-2}}. \quad (9)$$

According to Jaroniec (1993) [57], the following relationship between the micropore size distribution function $J(x)$ and the micropore dimension x is proposed:

$$\ln J(x) = (2 - D)\ln x + C. \quad (10)$$

In summary, the steps to calculate the fractal dimension of micropores by using CO₂ adsorption data are as follows: First, the adsorption volume data are obtained by using CO₂ adsorption data and the DR equation; then, the parameters ρ and v are obtained by nonlinear fitting, z is calculated by using the pore size distribution data, and then Equation (9) is applied to obtain the pore size distribution function $J(x)$. Finally, $\ln x$ and $\ln J(x)$ are fitted by Equation (10) to obtain the slope of the logarithmic curve, and the fractal dimension D of micropores is further obtained.

Figure 7 shows the fitting curves of $\ln x$ and $\ln J(x)$ of the CO₂ adsorption samples. The linear fitting slope, correlation coefficient (R^2) and fractal dimension of each sample are shown in the Table 4, and R^2 is greater than 0.91. The D values of all coal and rock samples are distributed between 2 and 3, which proves that they conform to fractal theory. The D values are distributed between 2.4441 and 2.6646, with an average of 2.603, which is basically the same as the results of Xiong et al. (2020) from their study on the coal of the Shanxi, Taiyuan and Benxi Formations in the eastern Ordos Basin (D value is 2.63–2.80, with an average value of 2.75) and the results of Li et al. (2019) from their study on lean coal and anthracite in the Qinshui Basin (D values are 2.38–2.63 and 2.31–2.68, respectively) [44,54,59].

4.5. Methane Adsorption Characteristics

Numerous HPMA studies on coal have shown that the Langmuir equation is the most straightforward and widely accepted model to describe the relationship between the gas pressure and the amount of CH₄ adsorbed on coal [60–63]. According to Langmuir theory, the outer surface of the coal sample is uniform in terms of energy, CH₄ molecules are absorbed only on the outer surface of the coal sample in the form of a monolayer covering, and the adsorption amount of CH₄ depends on the SSA of the outer surface [64,65]. The results show that the Langmuir volume (V_L) and Langmuir pressure (P_L) ranges of the seven selected coal samples are 24.46~32.83 m³/t and 2.91~3.46 MPa, respectively (Figure 8). Among them, the V_L and P_L of PM-7 are the largest, and the corresponding SSA and PV of PM-7 are large, indicating that the micropores are well developed and provide a large

amount of SSA. The V_L and P_L of PM-1 are the smallest, and the corresponding micro-SSA and micro-PV are small. Previous studies have shown that the adsorbent–adsorptive interaction in micropores is enhanced; thus, CH₄ molecules are adsorbed only in the microporous structure in the form of micropore filling, and the adsorption capacity of CH₄ is limited by the micro-PV [35,38].

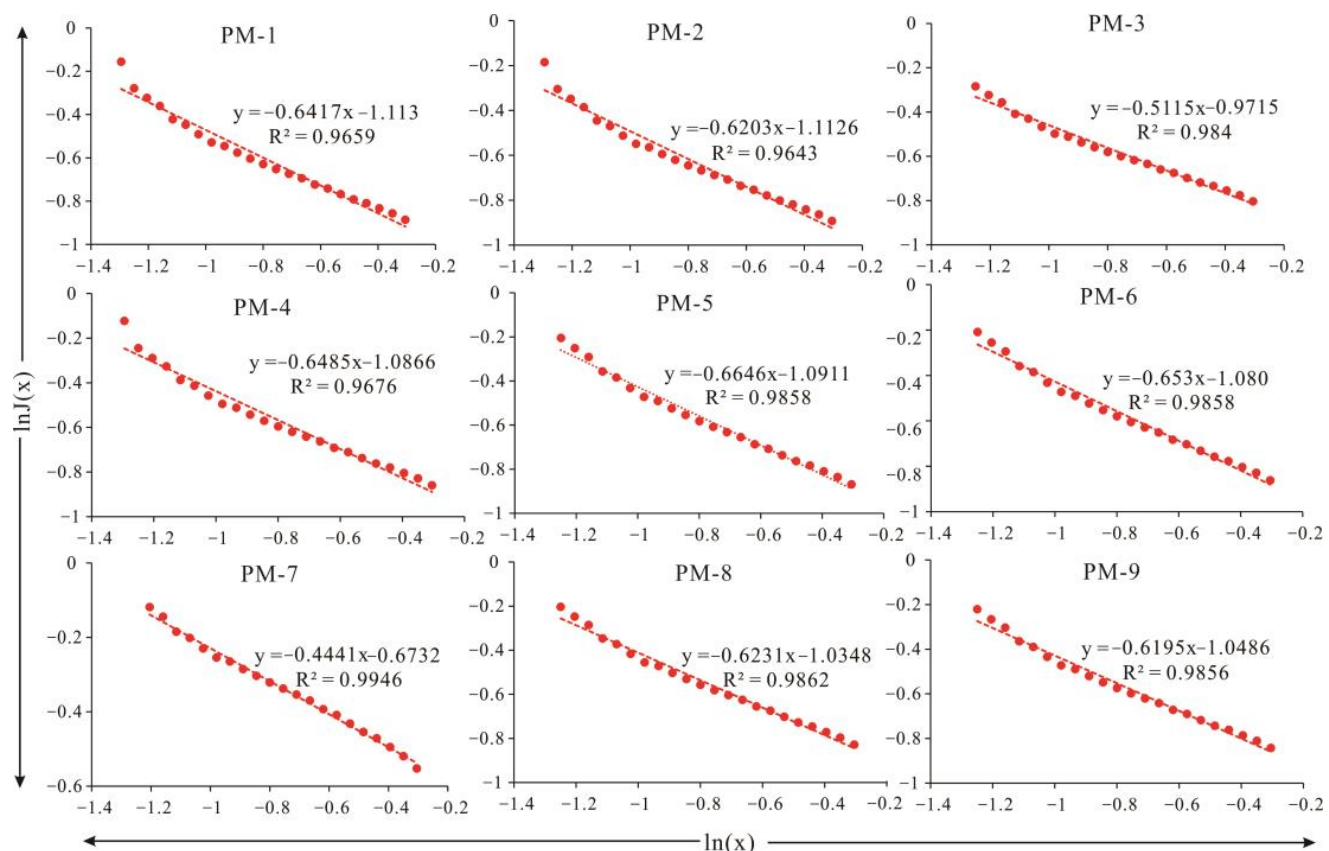


Figure 7. Fractal dimension fitting of the CO₂ adsorption data of coal samples.

Table 4. Fractal dimension of the CO₂ adsorption data of coal samples.

Samples	Fitting Equation	Slope	Fractal Dimension	Degree of Fitting
PM-1	$\ln J(x) = -0.6417 \ln x - 1.113$	-0.6417	2.6417	0.9659
PM-2	$\ln J(x) = -0.6203 \ln x - 1.1126$	-0.6203	2.6203	0.9643
PM-3	$\ln J(x) = -0.5115 \ln x - 0.9715$	-0.5115	2.5115	0.984
PM-4	$\ln J(x) = -0.6485 \ln x - 1.0866$	-0.6485	2.6485	0.9676
PM-5	$\ln J(x) = -0.6646 \ln x - 1.0911$	-0.6646	2.6646	0.9858
PM-6	$\ln J(x) = -0.6530 \ln x - 1.0800$	-0.653	2.653	0.9858
PM-7	$\ln J(x) = -0.4441 \ln x - 0.6732$	-0.4441	2.4441	0.9946
PM-8	$\ln J(x) = -0.6231 \ln x - 1.0348$	-0.6231	2.6231	0.9862
PM-9	$\ln J(x) = -0.6195 \ln x - 1.0486$	-0.6195	2.6195	0.9856

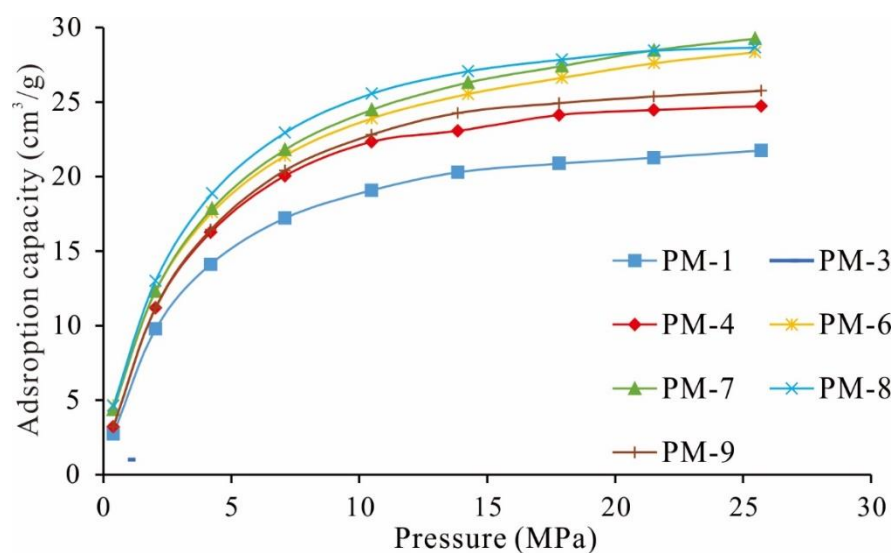


Figure 8. Isothermal adsorption curves of seven selected coal samples.

5. Discussion

5.1. Development and Pore Size Distribution of Micropores

LPA data can be calculated based on the NLDFT model to obtain the SSA, PV, PSD and other relevant information of the effective pore size range of 0.3~1.5 nm. LTA data can be calculated based on the NLDFT model to obtain the SSA, PV, PSD and other relevant information of the effective pore size measurement range of 1.06~77.7 nm. The overlap of the two models is 1.06~1.50 nm. Since the results of the two experiments are different in the overlap range [9], the arithmetic mean of the two models is used in this paper to determine the PV, SSA and PSD in the range of 1.06~1.50 nm. The PV, SSA and PSD of micropores were calculated by LTA and LPA (Figure 9a,b). The micro-PV and micro-SSA values of the coal samples range from 0.059 to 0.086 cm³/g and from 204.380 to 282.415 m²/g, respectively. These results show that the coal samples in the study area are extremely well developed, and the micro-PV in coal is several hundred times higher than that of marine shale in the Sichuan Basin and transitional facies in the Ordos Basin [44,54,63] but close to that of coal in eastern Yunnan [13].

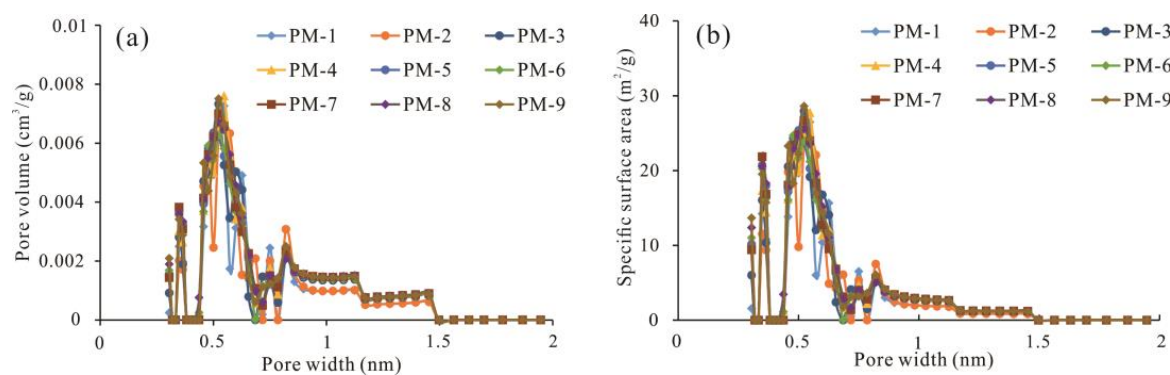


Figure 9. Distributions of the PV and SSA results of different sizes of micropores. (a) PV; (b) SSA.

Although the size range of micropores is very small, the PSD shows a certain regularity [9,20]. As shown in Figure 9a,b, the PSD has multiple peaks, which are mainly in the ranges of 0.3–0.4 nm, 0.4–0.7 nm and 0.7–2.0 nm. Among them, the degree of development of nanopores in the coal samples is similar. The PV and SSA of 0.4–0.7 nm are the most developed, accounting for more than 60% of the PV and SSA (Table 5 and Figure 10). The PV and SSA in the pore size range of 0.7–2.0 nm follow, and the PV and SSA in the pore

size range of 0.3–0.4 nm are the least developed. The PSD of coal rock is similar to that of activated carbon and shale at pore sizes < 1.0 nm, but the PV and SSA of coal rock at pore sizes of 1.0–2.0 nm are significantly lower than those of activated carbon and higher than those of shale [9,56,66].

Table 5. PV and SSA results of different sizes of micropores.

Samples	PV (cm^3/g)			SSA (m^2/g)		
	<0.4 nm	0.4–0.7 nm	0.7–2.0 nm	<0.4 nm	0.4–0.7 nm	0.7–2.0 nm
PM-1	0.0047	0.039	0.0153	26.66	145.66	32.06
PM-2	0.0053	0.0416	0.0161	30.93	154.63	33.83
PM-3	0.0083	0.0449	0.021	48.15	167.48	43.05
PM-4	0.0073	0.044	0.0213	42.48	163.59	44
PM-5	0.0085	0.0435	0.0204	48.86	162.25	41.99
PM-6	0.0082	0.0414	0.0207	47.48	155.15	43.14
PM-7	0.0068	0.0482	0.0308	38.6	178.78	65.05
PM-8	0.0088	0.0465	0.0211	51.19	173.51	43.51
PM-9	0.0084	0.0443	0.0216	48.94	165.89	45.03

Note: PV = pore volume; SSA = specific surface area.

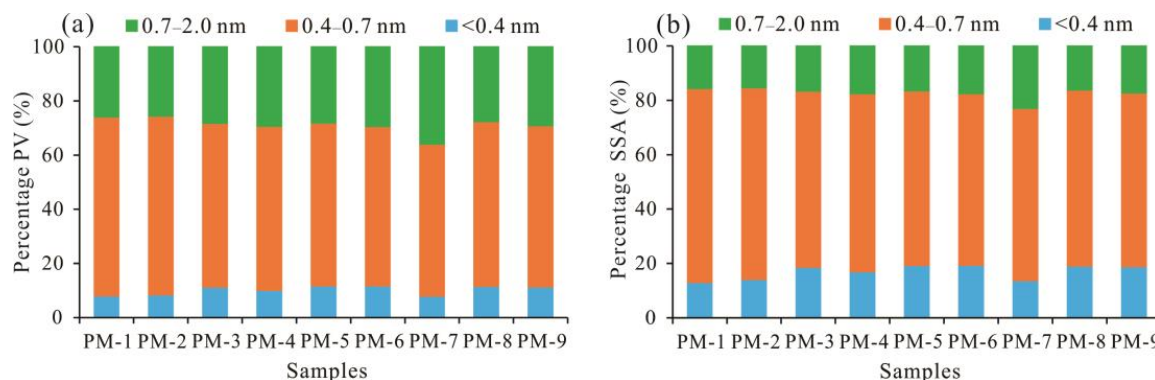


Figure 10. Distributions of different pore sizes acquired from CO_2/N_2 adsorption in terms of the (a) percentage of pore volume and (b) percentage of SSA.

5.2. Proportion of Micropores in Total Pores

Micropores are widely distributed and abundant in coal and are usually the main space for gas adsorption and initial gas migration in coal seams. The qualitative and quantitative description of micropore development characteristics can play a very important role in determining the scale and form of gas migration in coal, so it is necessary to further analyse and study the development scale, pore morphology and pore structure of coal micropores.

To explore the contribution degree of micropores to the total PV and total SSA of pores in coal, the above established quantitative characterization method of pores in coal was used to calculate the total PV and total SSA of pores in the pore size range of 0.3–100 nm. The results are shown in Figure 11 and Table 6, and the proportions of nano-PVs and SSAs are different for different pore size ranges. The micro-PVs contribute 97.25%~99.03%, with an average of 98.18%. The meso-PV contributes 0.92%~2.31%, with an average of 1.60%. The macro-PV contributes 0.05%~0.44%, with an average of 0.21%. These results indicate that the contribution of PV in coal mainly originates from micropores, while the contribution of mesopores and macropores is relatively small. The micro-SSA contributes 99.79%~99.90%, with an average of 99.84%. The meso-SSA contributes 0.10%~0.21%, with an average of 0.16%. These results indicate that the contribution of SSA in coal mainly

originates from the micropores, followed by the mesopores, and the contribution of the macropores can be ignored. As shown in Figure 10a,b, the distribution trend of PV and SSA of the same coal sample has a good consistency, and the pore SSA of the pore segment with PV development also develops. In coal sample, both PV and SSA are mainly contributed by micropores. These results indicate that the large number of micropores with large surface are the main adsorption and occurrence sites of CBM, as well as the effective channels for initial migration and diffusion of CBM after desorption, so it is necessary to further study and analyze their development and structural characteristics.

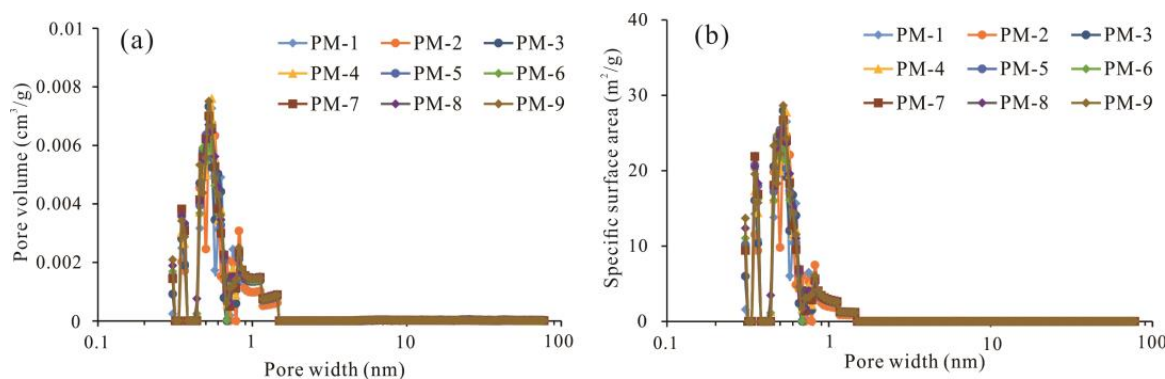


Figure 11. PV and SSA rates of change for all the pore sizes by using two models: (a) pore volume, (b) specific surface area.

Table 6. The PV, SSA and proportions of micro, meso-, and macropores in different coals.

Samples	PV (cm³/g)			SSA (m²/g)			PV Proportion (%)			SSA Proportion (%)		
	Micro	Meso	Macro	Micro	Meso	Macro	Micro	Meso	Macro	Micro	Meso	Macro
PM-1	0.0591	0.0011	0.0002	204.38	0.38	0.01	97.89	1.81	0.31	99.81	0.18	0.01
PM-2	0.063	0.0009	0.0001	219.39	0.34	0.01	98.35	1.48	0.17	99.83	0.16	0.01
PM-3	0.0742	0.001	0.0002	258.68	0.33	0.01	98.47	1.3	0.23	99.86	0.13	0.01
PM-4	0.0726	0.0014	0.0001	250.07	0.52	0.01	97.95	1.92	0.12	99.78	0.21	0.01
PM-5	0.0724	0.0017	0.0003	253.1	0.46	0.02	97.25	2.31	0.44	99.81	0.18	0.01
PM-6	0.0703	0.0013	0.0001	245.77	0.44	0.01	98.06	1.78	0.16	99.81	0.18	0.01
PM-7	0.0858	0.0008	0.0001	282.42	0.28	0.01	99.03	0.92	0.05	99.89	0.1	0.01
PM-8	0.0765	0.0011	0.0002	268.21	0.38	0.01	98.28	1.43	0.29	99.85	0.14	0.01
PM-9	0.0743	0.0011	0.0001	259.86	0.41	0.01	98.36	1.48	0.16	99.83	0.16	0.01

Note: PV = pore volume; SSA = specific surface area; Micro = micropores; Meso = mesopores; Macro = macropores.

5.3. Pore Structural Parameters and Fractal Dimensions

Previous studies on the factors influencing the pore structure of coal rock suggest that coal rank and coal composition (moisture, ash, vitrinite and mineral composition) are the main factors controlling PV and SSA [9,10,13,20]. As shown in Figure 12a, there is no significant correlation between the micro-PV and micro-SSA results of coal samples and vitrinite content. This finding differs from those of previous studies [10,18]; this difference may be due to the small number of samples and narrow reflectivity range between samples. The micro-PV and micro-SSA are negatively correlated with the mineral content in coal samples. There are two main aspects: on the one hand, the minerals can form pores; on the other hand, minerals can fill some of the existing pores, resulting in a decrease in the PV and SSA (Figure 12d), which is consistent with the results of previous studies [11,54]. The relationships between the micro-PV and micro-SSA and proximate analysis parameters (M_{ad} and A_{ad}) are shown in Figure 12c,d, and there is no obvious relationship between the

micro-PV or micro-SSA and M_{ad} . Due to the relatively low water content of coal and rock in the study area, there is no correlation between the micro-PV or micro-SSA and M_{ad} . The micro-PV and micro-SSA show linear negative correlations with A_d . As A_d is a derivative of the minerals in coal, it is formed by complex reactions, such as de-composition and combination reactions [13]. The negative correlations of PV, SSA and A_d are consistent with that of mineral content, that is, the development of pores in these samples is controlled by both the organic matter and mineral content; and minerals can increase the value of A_d . When the minerals in coal fill in some of the pores, this leads to decreases in PV and SSA.

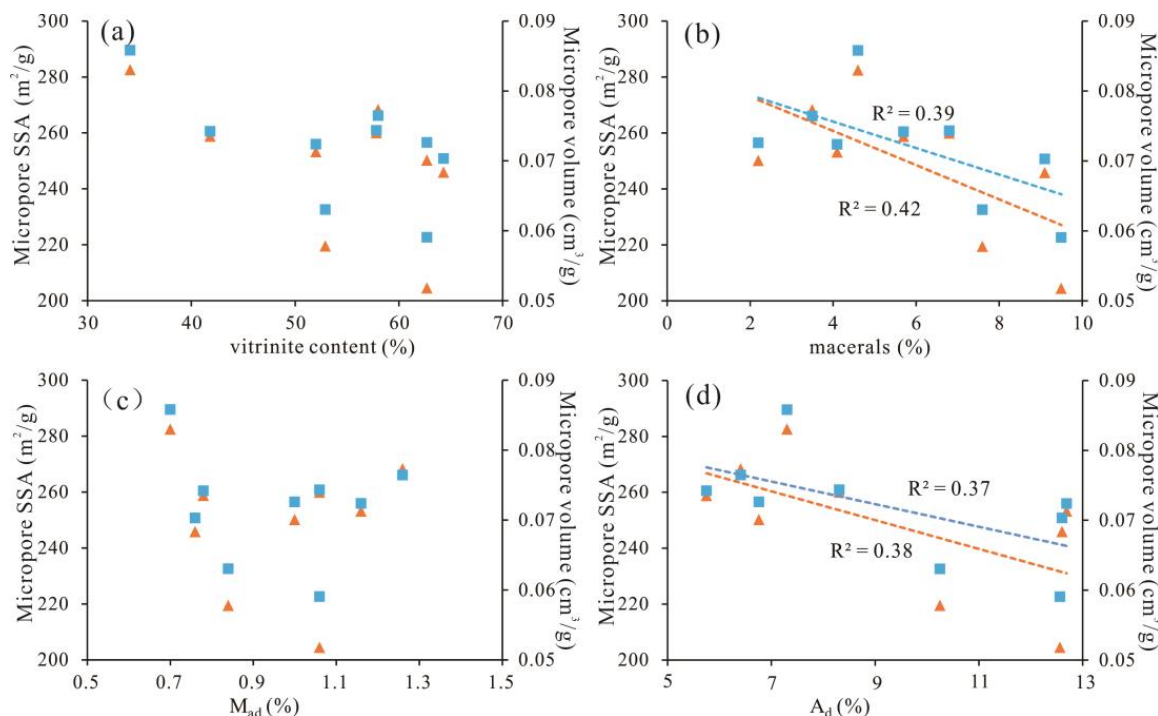


Figure 12. Relationships between the micro-PV, micro-SSA and (a) vitrinite content, and (b) macerals, (c) M_{ad} , and (d) V_d .

5.4. Influence on the Fractal Dimensions

To investigate the influence of the maceral composition and proximate analysis parameters on deep coal micropores fractal dimensions, the related plots are illustrated in Figure 13. The D value increases with increasing vitrinite content (Figure 13a), indicating that vitrinite has a positive effect on the fractal dimension. This result is consistent with the views of Clarkson and Bustin (2008) and Fu et al. (2017) [66–69]. The higher the content of vitrinite in the coal samples, the more micropores tend to develop. As the mineral component content increases, the D value shows no obvious trend of change (Figure 13b). Due to the relatively low mineral content of coal samples in the study area, there is no obvious correlation between the fractal dimension of micropores and mineral components. There is a weak positive correlation between the D value and M_{ad} (Figure 13c), which may be because a higher M_{ad} of the coal sample indicates that the water molecules in the gas–liquid phase form tension on the pore surface of the coal, thus exerting a great influence on the fractal dimension [51,70]. The positive correlation between D and A_d is weak (Figure 13d); as A_d increases, the coal pore structure becomes complicated. Yao et al. (2012) believed that ash in coal would fill the pores, resulting in the enhancement of the heterogeneity of the coal pore structure and an increase in the fractal dimension [24]. In conclusion, due to the relatively low mineral content, its influence on the fractal dimension of pores is limited. The influences of A_d and M_{ad} on the fractal dimension of coal pores are not obvious, indicating that the factors controlling the fractal dimension of deep coal pores are more complex and

may be affected by many factors. The factors controlling the pore fractal dimension of deep coal rocks need to be studied in more detail in the future.

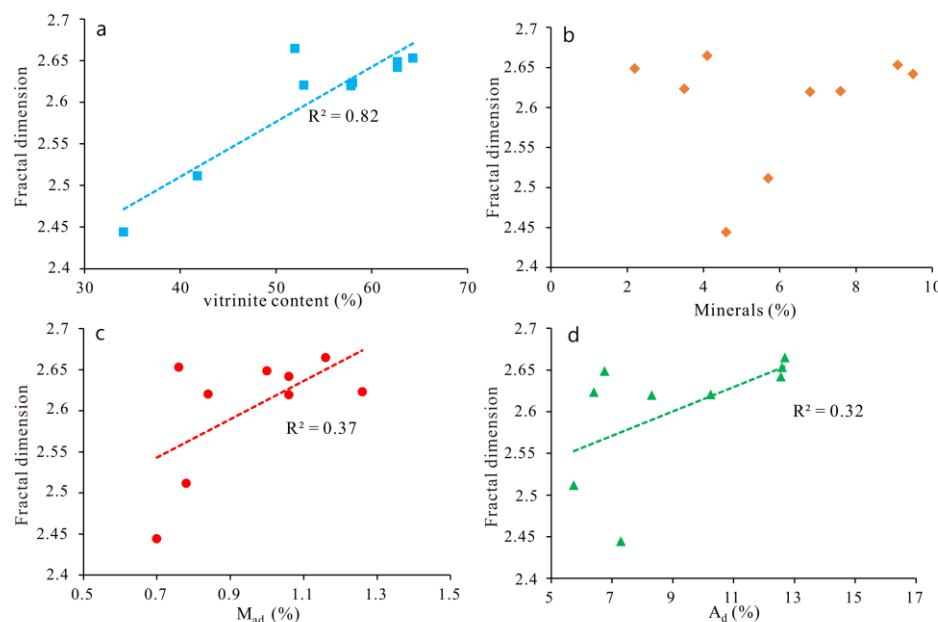


Figure 13. Relationship between the micropore fractal dimension and vitrinite content (a), and minerals (b), d M_{ad} (c) and A_d (d).

This study shows that the pores of coal are mainly micropores, the micro-PV and micro-SSA contribute more than 90% of the total pores, and the mesopores and macropores are rarely or almost undeveloped [22,71]. Mesopores and macropores are mainly developed in shale pores, occupying approximately 90% of the total PV and 60% of the total SSA [10,72]. Figure 14 shows the relationship between the fractal dimension (D) and pore structure parameters. D has a negative linear correlation with the micro-SSA and micro-PV, but the correlation is poor, which may be caused by the high heterogeneity of coal and rock samples. This result is consistent with coal sample data obtained by Xiong et al. (2020). The fractal dimension of micropores decreases with the increase in the micro-SSA and micro-PV, indicating that the smaller the storage space and SSA of pores, the stronger the homogeneity of coal and rock, and the more complex the pore structure.

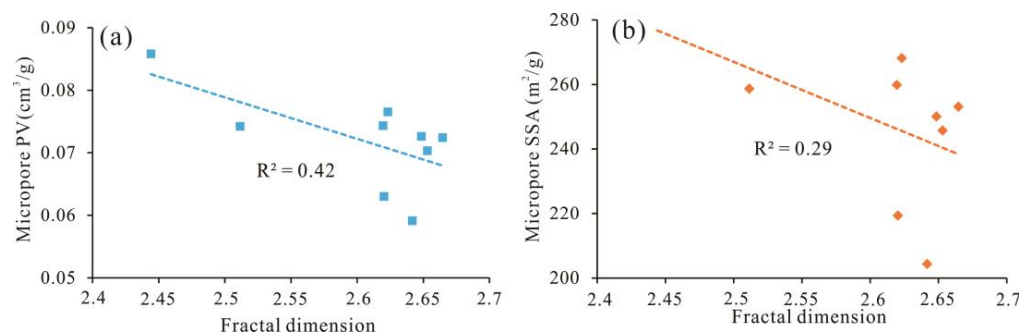


Figure 14. Relationships between the micropore fractal dimension and (a) micro-PV and (b) micro-SSA.

5.5. Adsorption Capacity of Micropores

CBM is mainly retained on the inner surfaces of coal micropores in the adsorbed state, so the SSA of coal is of great significance to its adsorption capacity and enrichment characteristics [7,20]. According to the basic physical adsorption theory of solid surfaces, the adsorption capacity of an object is proportional to the SSA [9]. Zhong et al. (2002)

conducted LTA and methane adsorption experiments on coal samples and determined that the adsorption capacity of coal to CH_4 was positively correlated with the total PV, total SSA and micro-SSA [73]. Sang et al. (2003) determined that the SSA of coal was negatively correlated with the adsorption capacity [74]. Chen et al. (2017) discovered a strong linear positive correlation between CO_2 -SSA and V_L [20]. Regarding the cause of the difference, previous researchers have used different determination and precision methods of the SSA of coal [9,20]. Figure 15 shows scatter diagrams of the correlations between the V_L and the micro-PV and micro-SSA. V_L has an obvious positive linear correlation with micro-PV and micro-SSA (Figure 15b). This correlation shows that micropores have an obvious influence on the adsorption gas of coal and rock.

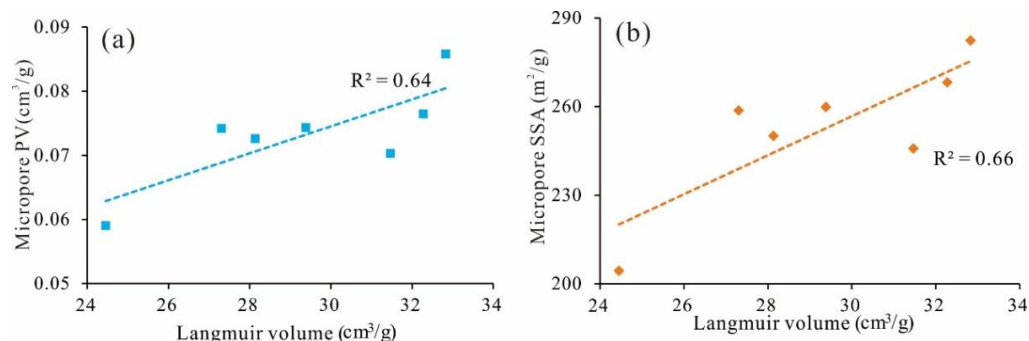


Figure 15. Relationships between the high-pressure CH_4 adsorption capacities and (a) micro-PV and (b) micro-SSA.

Table 6 shows that the contribution of the micro-SSA to the total SSA reaches 99%, indicating that methane is mainly absorbed in the micropores of a coal reservoir and that the gas adsorption capacity of a coal reservoir depends on the total PV and distribution frequency of pores in this part [20]. In addition, it is known that LPA absorbs carbon dioxide with a smaller molecular diameter than N_2 as the adsorbent, not only to avoid the disadvantage of carbon dioxide not being completely adsorbed when the micropore size is close to the molecular size of nitrogen, but also quickly reach adsorption equilibrium [20,75]; therefore, the SSA and PV of micropore can be accurately measured. This study shows that the combination of LPA and LTA can more accurately reveal the pore structure and adsorption capacity of coal reservoirs than either method, especially for micropores <2 nm in size.

6. Conclusions

This paper uses deep coal samples of the Daning–Jixian block from the eastern margin of the Ordos Basin as the research object. Using LPA and LTA experiments, FE-SEM and other pore structure analysis methods, a research method for the precise determination and quantitative characterization of micropores in coal is proposed. Considering fractal theory, the factors affecting the fractal dimension of micropores are discussed from the perspective of the physical properties of coal samples. HPMA experiments are carried out to explore the gas adsorption capacity of micropores. The following conclusions are drawn:

- (1) The LPA method based on the NLDFT model is the best method to measure and calculate the PV, SSA and PSD corresponding to the pore size range from 0.3~1.5 nm, as validated by comparing the results of the LPA and LTA experiments and different calculation models. Combining the LPA method with the LTA method based on the NLDFT model, all micropores smaller than 2.0 nm can be measured.
- (2) The pores developed in deep coal rocks are mainly organic pores, InterP pores and microfractures, and the pore size distribution patterns of different coal samples have multiple peaks, among which micropores are the main contributors to the total PV and total SSA, with the micro-PV ranging from 0.059 to 0.086 cm^3/g and the micro-SSA ranging from 204.380 to 282.415 m^2/g .

- (3) Different coal samples in the study area have great differences in the degree of micropore development, but the pore distribution characteristics are basically the same. The PV and SSA of the 0.4–0.7 nm pore size range are the most developed, accounting for more than 60%. Micropore structure development is mainly affected by the maceral and mineral components. With increasing mineral content and A_d , micro-PV and micro-SSA decrease rapidly.
- (4) The micropore fractal dimension (D) is calculated based on LPA data. The D values range from 2.4441 to 2.6646, with an average of 2.603. The relationship between the D value and mineral content is not obvious, but D is positively correlated with vitrinite content, M_{ad} and A_d .
- (5) The contribution rate of micro-SSA to total SSA of coal samples in the study area reaches 99%, and V_L is linearly positively correlated with micro-SSA, which shows that the adsorption capacity of coal reservoir depends on the development degree of micro-SSA.

Author Contributions: Conceptualization, T.W. and Z.D.; methodology, T.W. and H.H.; software, T.W.; validation, T.W., Z.D. and H.H.; formal analysis, T.W.; investigation, T.W. and F.T.; resources, Z.D.; data curation, Z.D.; writing—original draft preparation, T.W.; writing—review and editing, T.W.; visualization, T.W.; supervision, F.T.; project administration, F.T.; funding acquisition, Z.D. All authors have read and agreed to the published version of the manuscript.

Funding: This research was jointly supported by the Research and Experiment on Scale Benefit Development Technology of Deep Coalbed Methane in Daning-Jixian (Grant No. 2022KT1401) and In Situ Bio-gasification Mechanism and Experimental Study of Coalbed Methane (Grant No. 2021DJ2302). We thank PetroChina Exploration and Development Research Institute and PetroChina Coalbed Methane Company Limited for picking up the samples.

Data Availability Statement: The data used to support the findings of this study are included within the article.

Acknowledgments: We thank PetroChina Exploration and Development Research Institute and PetroChina Coalbed Methane Company Limited for picking up the samples.

Conflicts of Interest: The authors declare no conflict of interest.

References

1. Blacher, S.; Sahouli, B.; Heinrichs, B.; Lodewyckx, P.; Pirard, R.; Pirard, J.P. Micropore size distributions of activated carbons. *Langmuir* **2000**, *16*, 6754–6756. [[CrossRef](#)]
2. Tao, S.; Chen, S.; Tang, D.; Zhao, X.; Xu, H.; Li, S. Material composition, pore structure and adsorption capacity of low-rank coals around the first coalification jump: A case of eastern Junggar Basin, China. *Fuel* **2018**, *211*, 804–815. [[CrossRef](#)]
3. Sing, K.S.W.; Everett, D.H.; Haul, R.A.W. Reporting physisorption data for gas/solid systems with special reference to the determination of surface area and porosity. *Pure Appl. Chem.* **1985**, *57*, 603–619. [[CrossRef](#)]
4. Cui, X.; Bustin, R.M.; Dipple, G. Selective transport of CO₂, CH₄, and N₂ in coals: Insights from modeling of experimental gas adsorption data. *Fuel* **2004**, *83*, 293–303. [[CrossRef](#)]
5. Groen, J.C.; Peffer, L.A.; Pérez-Ramírez, J. Pore size determination in modified microand mesoporous materials. Pitfalls and limitations in gas adsorption data analysis. *Microporous Mesoporous Mater.* **2003**, *60*, 1–17. [[CrossRef](#)]
6. Hou, S.; Wang, X.; Wang, X.; Yuan, Y.; Pan, S.; Wang, X. Pore structure characterization of low volatile bituminous coals with different particle size and tectonic deformation using low pressure gas adsorption. *Int. J. Coal Geol.* **2017**, *183*, 1–13. [[CrossRef](#)]
7. Hu, B.; Cheng, Y.; He, X.; Wang, Z.; Wang, L.; Jiang, Z.; Wang, C.; Wei, L.; Wang, L. New insights into the CH₄ adsorption capacity of coal based on microscopic pore properties. *Fuel* **2019**, *262*, 116675. [[CrossRef](#)]
8. Li, C.; Jiang, B.; Ju, W.; Cheng, G.; Song, Y. Characteristics of tectonic deformation in the Daning-Jixian region, eastern Ordos Basin: Implications for the exploration and development of coalbed methane. *Energy Explor. Exploit.* **2019**, *37*, 907–921. [[CrossRef](#)]
9. Song, D.; Ji, F.; Li, Y.; Zhao, H.; Song, B.; He, K. Heterogeneous development of micropores in medium-high rank coal and its relationship with adsorption capacity. *Int. J. Coal Geol.* **2020**, *226*, 103497. [[CrossRef](#)]
10. Ma, X.; Guo, S.; Shi, D.; Zhou, Z.; Liu, G. Investigation of pore structure and fractal characteristics of marine-continental transitional shales from Longtan Formation using MICP, gas adsorption, and NMR (Guizhou, China). *Mar. Pet. Geol.* **2019**, *107*, 555–571. [[CrossRef](#)]
11. Li, G.; Qin, Y.; Wu, M.; Zhang, B.; Wu, X.; Tong, G.; Liu, J. The pore structure of the transitional shale in the Taiyuan formation, Linxing area, Ordos Basin. *J. Pet. Sci. Eng.* **2019**, *189*, 106183. [[CrossRef](#)]
12. Lu, W.; Zhuang, Z.; Zhang, W.; Zhang, C.; Song, S.; Wang, R.; Kong, B. Study on the Pore and Crack Change Characteristics of Bituminous Coal and Anthracite after Different Temperature Gradient Baking. *Energy Fuels* **2021**, *35*, 19448–19463. [[CrossRef](#)]

13. Zhang, S.; Wu, C.; Liu, H. Comprehensive characteristics of pore structure and factors influencing micropore development in the Laochang mining area, eastern Yunnan, China. *J. Pet. Sci. Eng.* **2020**, *190*, 107090. [[CrossRef](#)]
14. Wei, Y.; Li, J.; Du, Y.; Lu, S.; Li, W.; Yang, J.; Feng, W.; Song, Z.; Zhang, Y. Classification Evaluation of Gas Shales Based on High-Pressure Mercury Injection: A Case Study on Wufeng and Longmaxi Formations in Southeast Sichuan, China. *Energy Fuels* **2021**, *35*, 9382–9395. [[CrossRef](#)]
15. Chalmers, G.R.; Bustin, R.M.; Power, I.M. Characterization of gas shale pore systems by porosimetry, pycnometry, surface area, and field emission scanning electron microscopy/transmission electron microscopy image analyses: Examples from the Barnett, Woodford, Haynesville, Marcellus, and Doig units. *AAPG Bull.* **2012**, *96*, 1099–1119.
16. Zhou, S.; Liu, D.; Cai, Y.; Karpyn, Z.; Yao, Y. Comparative analysis of nanopore structure and its effect on methane adsorption capacity of Southern Junggar coalfield coals by gas adsorption and FIB-SEM tomography. *Microporous Mesoporous Mater.* **2018**, *272*, 117–128. [[CrossRef](#)]
17. Li, Z.; Liu, D.; Cai, Y.; Wang, Y.; Teng, J. Adsorption pore structure and its fractal characteristics of coals by N₂ adsorption/desorption and FESEM image analyses. *Fuel* **2019**, *257*, 116031. [[CrossRef](#)]
18. Wang, X.; Jiang, Z.; Shu, S.; Chang, J.; Zhu, L.; Li, X.; Li, J. Full-Scale Pore Structure and Fractal Dimension of the Longmaxi Shale from the Southern Sichuan Basin: Investigations Using FE-SEM, Gas Adsorption and Mercury Intrusion Porosimetry. *Minerals* **2019**, *9*, 3–26. [[CrossRef](#)]
19. Mastalerz, M.; Drobniak, A.; Rupp, J. Meso-and micropore characteristics of coal lithotypes: Implications for CO₂ adsorption. *Energy Fuels* **2008**, *22*, 4049–4061. [[CrossRef](#)]
20. Chen, S.; Tao, S.; Tang, D.; Xu, H.; Li, S.; Zhao, J.; Jiang, Q.; Yang, H. Pore structure characterization of different rank coals using N₂ and CO₂ adsorption and its effect on CH₄ adsorption capacity: A case in Panguan Syncline, Western Guizhou, China. *Energy Fuels* **2017**, *31*, 6034–6044. [[CrossRef](#)]
21. Li, Y.; Song, D.; Liu, S.; Pan, J. Characterization of Ultra-Micropores and Analysis of Their Evolution in Tectonically Deformed Coals by Low-Pressure CO₂ Adsorption, XRD and HRTEM Techniques. *Energy Fuels* **2020**, *34*, 9436–9449. [[CrossRef](#)]
22. Han, W.; Zhou, G.; Gao, D.; Zhang, Z.; Wei, Z.; Wang, H.; Yang, H. Experimental analysis of the pore structure and fractal characteristics of different metamorphic coal based on mercury intrusionnitrogen adsorption porosimetry. *Powder Technol.* **2020**, *362*, 386–398. [[CrossRef](#)]
23. Ma, Y.; Wang, M.; Zhao, X.; Dai, X.; He, Y. Study of the Microstructural Characteristics of Low-Rank Coal under Different Degassing Pressures. *Energies* **2022**, *15*, 3691. [[CrossRef](#)]
24. Yao, Y.; Liu, D. Comparison of low-field NMR and mercury intrusion porosimetry in characterizing pore size distributions of coals. *Fuel* **2012**, *95*, 152–158. [[CrossRef](#)]
25. Okolo, G.N.; Everson, R.C.; Neomagus, H.W.J.P.; Roberts, M.J.; Sakurovs, R. Comparing the porosity and surface areas of coal as measured by gas adsorption, mercury intrusion and SAXS techniques. *Fuel* **2015**, *141*, 293–304. [[CrossRef](#)]
26. Zhao, Y.; Sun, Y.; Liu, S.; Chen, Z.; Yuan, L. Pore structure characterization of coal by synchrotron radiation nano-CT. *Fuel* **2018**, *215*, 102–110. [[CrossRef](#)]
27. Yu, S.; Bo, J.; Meijun, Q. Molecular dynamic simulation of self-and transport diffusion for CO₂/CH₄/N₂ in low-rank coal vitrinite. *Energy Fuel* **2018**, *32*, 3085–3096. [[CrossRef](#)]
28. Amarasekera, G.; Scarlett, M.J.; Mainwaring, D.E. Micropore size distributions and specific interactions in coals. *Fuel* **1995**, *74*, 115–118. [[CrossRef](#)]
29. Clarkson, C.R.; Bustin, R.M. Variation in micropore capacity and size distribution with composition in bituminous coal of the Western Canadian Sedimentary Basin: Implications for coalbed methane potential. *Fuel* **1996**, *75*, 1483–1498. [[CrossRef](#)]
30. Centeno, T.A.; Stoeckli, F. The assessment of surface areas in porous carbons by two model-independent techniques, the DR equation and DFT. *Carbon* **2010**, *48*, 2478–2486. [[CrossRef](#)]
31. Landers, J.; Gor, G.Y.; Neimark, A.V. Density functional theory methods for characterization of porous materials. *Colloids Surf. A Physicochem. Eng. Asp.* **2013**, *437*, 3–32. [[CrossRef](#)]
32. Zhu, H.; Ju, Y.; Lu, W.; Han, K.; Qi, Y.; Neupane, B. The characteristics and evolution of micro-nano scale pores in shales and coals. *J. Nanosci. Nanotechnol.* **2017**, *17*, 6124–6138. [[CrossRef](#)]
33. Guo, S.B.; Mao, W.J. Division of diagenesis and pore evolution of a Permian Shanxi shale in the Ordos Basin, China. *J. Pet. Sci. Eng.* **2019**, *182*, 920–9105. [[CrossRef](#)]
34. Kuang, L.; Dong, D.; He, W.; Wen, S.; Sun, S.; Li, S.; Qiu, Z.; Liao, X.; Li, Y.; Wu, J.; et al. Geological characteristics and development potential of transitional shale gas in the east margin of the Ordos Basin, NW China. *Pet. Explor. Dev.* **2020**, *47*, 471–482. [[CrossRef](#)]
35. Liu, Y.; Zhu, Y.; Liu, S.; Chen, S.; Li, W.; Wang, Y. Molecular structure controls on micropore evolution in coal vitrinite during coalification. *Int. J. Coal Geol.* **2018**, *199*, 19–30. [[CrossRef](#)]
36. Liu, C.; Zhong, J.; Wang, X.; Cao, M.; Wu, J.; Zhang, S.; Wu, X.; Sun, N.; Du, Y.; Liu, Y. Petrological characteristics and the impact of mineral content on reservoir quality in coal-bearing strata of Linxing area, eastern margin of Ordos Basin, China. *Energy Explor. Exploit.* **2018**, *36*, 872–894. [[CrossRef](#)]
37. Zhao, L.P.; Lu, J.; Li, X.; Li, Y.; He, Q.; Ma, Z. Logging calculation method and application of geochemical parameters of source rocks with different lithologies in marine-continental transitional facies in Ordos Basin, China. *Arab. J. Geosci.* **2022**, *15*, 1111. [[CrossRef](#)]

38. Zhang, M.; Fu, X. Characterization of pore structure and its impact on methane adsorption capacity for semi-anthracite in Shizhuangnan Block, Qinshui Basin. *J. Nat. Gas Sci. Eng.* **2018**, *53*, 370–384. [[CrossRef](#)]
39. Loucks, R.G.; Reed, R.M.; Ruppel, S.C.; Jarvie, D.M. Morphology, Genesis, and Distribution of Nanometer-scale Pores in Siliceous Mudstones of the Mississippian Barnett Shale. *J. Sediment. Res.* **2009**, *79*, 848–861. [[CrossRef](#)]
40. Wang, Y.; Liu, D.; Cai, Y.; Li, X. Variation of petrophysical properties and adsorption capacity in different rank coals: An experimental study of coals from the Junggar, Ordos and Qinshui Basins in China. *Energies* **2019**, *12*, 986. [[CrossRef](#)]
41. Ravikovich, P.I.; Haller, G.L.; Neimark, A.V. Density functional theory model for calculating pore size distributions: Pore structure of nanoporous catalysts. *Adv. Colloid Interface Sci.* **1998**, *76*, 203–226. [[CrossRef](#)]
42. Mahamud, M.; Lopez, O.; Pis, J.J.; Pajares, J.A. Textural characterization of coals using fractal analysis. *Fuel Process. Technol.* **2003**, *81*, 127–142. [[CrossRef](#)]
43. Thommes, M.; Kaneko, K.; Neimark, A.V.; Olivier, J.P.; Rodriguez-Reinoso, F.; Rouquerol, J. Physisorption of gases, with special reference to the evaluation of surface area and pore size distribution (IUPAC Technical Report). *Pure Appl. Chem.* **2015**, *87*, 1051–1069. [[CrossRef](#)]
44. Li, Y.; Wang, Z.; Pan, Z.; Niu, X.; Meng, S. Pore structure and its fractal dimensions of transitional shale: A cross-section from east margin of the Ordos Basin, China. *Fuel* **2019**, *241*, 417–431. [[CrossRef](#)]
45. Dubinin, M.M. Adsorption in micropores. *J. Colloid Interface Sci.* **1967**, *23*, 487–499. [[CrossRef](#)]
46. Marsh, H.; Rand, B. The characterization of microporous carbons by means of the Dubinin-Radushkevich equation. *J. Colloid Interface Sci.* **1970**, *33*, 101–116. [[CrossRef](#)]
47. Evans, R.; Marconi, U.M.B.; Tarazona, P. Capillary condensation and adsorption in cylindrical and slit-like pores. *J. Chem. Soc.* **1986**, *82*, 1763–1787. [[CrossRef](#)]
48. Gelb, L.D.; Gubbins, K.E.; Radhakrishnan, R.; Sliwinska-Bartkowiak, M. Phase separation in confined systems. *Rep. Prog. Phys.* **1999**, *62*, 1573–1659. [[CrossRef](#)]
49. El-Merraoui, M.; Aoshima, M.; Kaneko, K. Micropore size distribution of activated carbon fiber using the density functional theory and other methods. *Langmuir* **2000**, *16*, 4300–4304. [[CrossRef](#)]
50. Ji, X.; Song, D.; Ni, X.; Li, Y.; Zhao, H. Coal Matrix Deformation and Pore Structure Change in High-Pressure Nitrogen Replacement of Methane. *Energies* **2018**, *11*, 2–18. [[CrossRef](#)]
51. Wei, Z.; Fu, X.; Hao, M.; Li, G.; Pan, J.; Niu, Q.; Zhou, H. Experimental insights into the adsorption-desorption of CH₄/N₂ and induced strain for medium-rank coals. *J. Petrol. Sci. Eng.* **2021**, *204*, 108705.
52. Jagiello, J.; Thommes, M. Comparison of DFT characterization methods based on N₂, Ar, CO₂, and H₂ adsorption applied to carbons with various pore size distributions. *Carbon* **2004**, *42*, 1227–1232. [[CrossRef](#)]
53. Pan, J.; Wang, K.; Hou, Q.; Niu, Q.; Wang, H.; Ji, Z. Micro-pores and fractures of coals analysed by field emission scanning electron microscopy and fractal theory. *Fuel* **2016**, *164*, 277–285. [[CrossRef](#)]
54. Zhang, J.; Li, X.; Wei, Q.; Sun, K.; Zhang, G.; Wang, F. Characterization of Full-Sized Pore Structure and Fractal Characteristics of Marine–Continental Transitional Longtan Formation Shale of Sichuan Basin, South China. *Energy Fuels* **2017**, *31*, 10490–10504. [[CrossRef](#)]
55. Jaroniec, M.; Lu, X.; Madey, R.; Choma, J. Evaluation of structural heterogeneities and surface irregularities of microporous solids. *Mater. Chem. Phys.* **1990**, *26*, 87–97. [[CrossRef](#)]
56. Machin, W.D. Temperature dependence of hysteresis and the pore size distributions of two mesoporous adsorbents. *Langmuir* **1994**, *10*, 1235–1240. [[CrossRef](#)]
57. Jaroniec, M.; Gilpin, R.K.; Choma, J. Correlation between microporosity and fractal dimension of active carbons. *Carbon* **1993**, *31*, 325–331. [[CrossRef](#)]
58. Stoeckli, H.F.; Ballerini, L.; Bernardini, S.D. On the evolution of micropore widths and areas in the course of activation. *Carbon* **2009**, *27*, 501–502. [[CrossRef](#)]
59. Xiong, Y.; Zhou, S.; Jiao, P.; Yang, M.; Zhou, J.; Wei, W.; Cai, J. Fractal analysis of micropore structures in coal and shale based on lowtemperature CO₂ adsorption. *Nat. Gas Geosci.* **2020**, *31*, 1028–1040.
60. Reucroft, P.J.; Sethuraman, A.R. Effect of pressure on carbon dioxide induced coal swelling. *Energy Fuels* **1987**, *1*, 72–75. [[CrossRef](#)]
61. Clarkson, C.R.; Bustin, R.M. The effect of pore structure and gas pressure upon the transport properties of coal: A laboratory and modeling study. 1. Isotherms and pore volume distributions. *Fuel* **1999**, *78*, 1345–1362. [[CrossRef](#)]
62. Li, J.; Li, B.; Ren, C.; Yang, K.; Zhang, Y. Characterization of Methane Adsorption Behavior on Wet Shale under Different Temperature Conditions. *Energy Fuels* **2020**, *34*, 2832–2848. [[CrossRef](#)]
63. Yang, Y.; Liu, S.; Zhao, W.; Wang, L. Intrinsic relationship between Langmuir sorption volume and pressure for coal: Experimental and thermodynamic modeling study. *Fuel* **2019**, *241*, 105–117. [[CrossRef](#)]
64. Langmuir, I. The adsorption of gases on plane surfaces of glass, mica and platinum. *J. Am. Chem. Soc.* **1918**, *40*, 1361–1403. [[CrossRef](#)]
65. Mosher, K.; He, J.; Liu, Y.; Rupp, E.; Wilcox, J. Molecular simulation of methane adsorption in micro-and mesoporous carbons with applications to coal and gas shale systems. *Int. J. Coal Geol.* **2013**, *109*, 36–44. [[CrossRef](#)]
66. Jia, A.; Hu, D.; He, S. Variations of Pore Structure in Organic-Rich Shales with Different Lithofacies from the Jiangdong Block, Fuling Shale Gas Field, SW China: Insights into Gas Storage and Pore Evolution. *Energy Fuels* **2020**, *34*, 12457–12475. [[CrossRef](#)]

67. Zhou, L.; Qian, Y.; Zhang, L.; Lan, X.; Wu, Y.; Wang, Q.; Zhang, G. Seismic prediction of oolithic beach thin-bed reservoir based on favorable facies belt constraints: Taking the second member of Feixianguan Formation in Jiulongshan area, Northwest Sichuan, China. *J. Nat. Gas Geosci.* **2021**, *6*, 329–344. [[CrossRef](#)]
68. Bustin, R.M.; Bustin, A.M.M.; Cui, X.; Ross, D.J.K.; Murthy, P.V.S. Impact of shale properties on pore structure and storage characteristics. In Proceedings of the Shale Gas Production Conference, Fort Worth, TX, USA, 16–18 November 2008.
69. Fu, H.J.; Tang, D.Z.; Xu, T.; Tan, S.; Yin, Z.Y.; Chen, B.L.; Zhang, C.; Wang, L.L. Characteristics of pore structure and fractal dimension of low-rank coal: A case study of Lower Jurassic Xishayao coal in the southern Junggar Basin, NW China. *Fuel* **2017**, *193*, 254–264. [[CrossRef](#)]
70. Shang, Z.; Dong, L.; Niu, L.; Shi, H. Adsorption of Methane, Nitrogen, and Carbon Dioxide in Atomic-Scale Fractal Nanopores by Monte Carlo Simulation I: Single-Component Adsorption. *Energy Fuels* **2019**, *33*, 10457–10475. [[CrossRef](#)]
71. Zhang, C.; Yao, Y.; Dong, Y. Heterogeneous development of micro- and meso-pores in shale kerogen: New insights from chemical structure analysis. *J. Nat. Gas Sci. Eng.* **2022**, *102*, 104552. [[CrossRef](#)]
72. Sun, Y.; Guo, S. Characterization of whole-aperture pore structure and its effect on methane adsorption capacity for transitional shales. *Energy Fuels* **2018**, *32*, 3176–3188. [[CrossRef](#)]
73. Zhong, L.W.; Zhang, H.; Yuan, Z.R.; Lei, C.L. Influence of specific pore area and pore volume of coal on adsorption capacity. *Coal Geol. Explor.* **2002**, *30*, 26–28.
74. Sang, S.X.; Qin, Y.; Guo, X.B.; Chen, Y.H. Storing characteristics of Jurassic coalbed gas in Junggar and Tuha Basins. *Geol. J. China Univ.* **2003**, *9*, 365–372.
75. Thommes, M.; Cychoz, K.A. Physical adsorption characterization of nanoporous materials: Progress and challenges. *Adsorption* **2014**, *20*, 233–250. [[CrossRef](#)]

Disclaimer/Publisher’s Note: The statements, opinions and data contained in all publications are solely those of the individual author(s) and contributor(s) and not of MDPI and/or the editor(s). MDPI and/or the editor(s) disclaim responsibility for any injury to people or property resulting from any ideas, methods, instructions or products referred to in the content.